PHYSICAL REVIEW A **97**, 043409 (2018)

Following coherent multichannel nuclear wave packets in pump-probe studies of O_2 with ultrashort laser pulses

Shan Xue,[1,2] Hongchuan Du,[1,*] Bitao Hu,[1] C. D. Lin,[2] and Anh-Thu Le[2,†]
[1]*School of Nuclear Science and Technology, Lanzhou University, Lanzhou 730000, China*
[2]*Department of Physics, Cardwell Hall, Kansas State University, Manhattan, Kansas 66506, USA*

(Received 12 March 2018; published 10 April 2018)

We reexamine the recent pump-probe experiment with O_2 using short intense infrared laser pulses theoretically. Using parameters that closely mimic the experimental conditions and taking into account the angle-dependent population redistribution due to resonant coupling between the relevant states, we show that the observed kinetic energy release spectra, including the energy-dependent structure and the quantum beat frequencies, can be accurately reproduced. Our results reveal additional important channels that were missed earlier. In particular, the strong contributions from ${O_2}^+$ $a\,^4\Pi_u$ and $b\,^4\Sigma_g^-$ states lead to the possibility of observing the interchannel beating. We further demonstrate that, by varying the laser parameters, the coherent nuclear wave-packet motions on different potential energy surfaces (PESs) can be probed and the properties of the PES can be examined. Future experiments with different wavelength lasers are proposed for better probing and controlling nuclear dynamics on different PESs.

DOI: 10.1103/PhysRevA.97.043409

I. INTRODUCTION

Coherent nuclear wave packets have been studied both experimentally and theoretically using the pump-probe technique for nearly three decades since the pioneering work by Zewail [1]. Early experiments were mostly limited to heavy or weakly bound molecules, for which the vibrational periods were typically of the order of picoseconds [2]. With the rapid progress of laser technology, tabletop infrared (IR) pulses of a few femtoseconds duration are now routinely available in the laboratory. Furthermore, high-order harmonics generated with intense short IR pulses can now serve as a coherent XUV source. These developments allow probing much faster nuclear motions in molecules with IR (or XUV) pump–IR probe techniques. In fact, vibrational dynamics of H_2 and D_2 have been extensively investigated; see, for example, Refs. [3,4]. Based on the success of these works in imaging ultrafast nuclear dynamics, one would generally expect somewhat straightforward extension of the method to other molecules. In practice, progress in this direction is rather slow. This is due to the fact that for more complex molecules, many channels are open in both pump and probe steps, either with strong IR or broadband XUV fields. Since many potential energy surfaces are at play, interpretation and theoretical simulation of the experimental data become increasingly difficult.

We note that recently developed techniques such as laser-induced electron diffraction (LIED) and high-harmonic generation spectroscopy have been shown to be capable of imaging molecular structures [5–9]. However, these techniques have been limited so far to static targets, except for a few notable cases where dynamics of simple molecules in the ground or low excited electronic states have been studied [10–13].

One of the main motivations for studying nuclear wave packets for molecules in intense laser fields is the possibility of identifying the relevant participating channels. Once the relevant channels have been identified, the properties of the associated potential energy surfaces (PESs) can be studied. An XUV-IR pump-probe measurement was reported quite recently for O_2 by Cörlin *et al.* [14]. An oscillation with a period of 40 fs was observed in a low-energy O^+ ion yield as a function of the pump-probe time delay. This feature was attributed to the vibrational wave-packet motion, launched by the pump pulse in the binding ${O_2}^+$ $a\,^4\Pi_u$ state, which is probed by absorption of an IR photon from the probe pulse to the weakly repulsive ${O_2}^+$ $f\,^4\Pi_g$ curve. In fact, by carefully analyzing theoretical simulations with different combinations of theoretical potential energy curves (PECs), a good set of PECs was identified, which gave overall good agreement with measured kinetic energy release (KER) and quantum beat (QB) spectra [14].

A similar attempt was made earlier by De *et al.* [15,16] in IR pump–IR probe experiments using intense few-cycle 800-nm laser pulses for diatomic molecules such as O_2, N_2, and CO. However, in contrast to Cörlin *et al.* [14], the identification of the relevant channels turned out to be quite intricate [16,17]. Indeed, in the case of O_2, the same ${O_2}^+$ $a\,^4\Pi_u$ and ${O_2}^+$ $f\,^4\Pi_g$ PECs were attributed as the main channels leading to the observed KER and QB spectra, as in Cörlin *et al.* [14]. However, the agreement between the experiment and theory was only fair. There are two notable discrepancies. First, the prominent energy-dependent structure in the observed KER spectra was not reproduced by the simulation [16,17]. Second, the positions of the theoretical QB frequencies (near 25 THz) were found to be shifted significantly with respect to the measured data (near 30 THz) [16]. These discrepancies are somewhat surprising, since the same states nicely reproduced the XUV-IR pump-

---

[*] duhch@lzu.edu.cn
[†] atle@phys.ksu.edu

probe experiments of Cörlin *et al.* [14], including the QB frequencies near 25 THz. These discrepancies remain largely unsolved in the newer simulations by Magrakvelidze *et al.* [17]. Naturally, these unsolved discrepancies raise some concerns about the difficulties and the applicability of this type of theoretical approach to more complex molecules.

In this paper we reexamine the IR pump–IR probe experiment of De *et al.* [16] for O_2. We show that all of the above discrepancies between the experiment and the early theoretical simulations [16,17] can be resolved. We found that the ${O_2}^+$ $b^4\Sigma_g^-$ state contributes significantly to the observed KER spectra. This state is expected to be weakly populated for molecules aligned perpendicularly to the laser polarization in a simple tunneling ionization model. Nevertheless, the resonant coupling with the more dominant ${O_2}^+$ $a\,^4\Pi_u$ state by the 800-nm pump pulse results in significant angle-dependent redistribution of both molecular states after the pump pulse. In contrast to the early works [16,17] where the simulations were carried out for molecules perfectly aligned along the laser polarization, our calculations take into account the realistic molecular alignment distribution. We also analyze the two other features of the observed KER spectra: the broad peak near 1.5 eV and the QB frequency near 48 THz. Finally, we address the possibility of probing the PES by varying the laser wavelength.

The paper is organized as follows. In Sec. II A we briefly describe our theoretical approach for solving the coupled-channel time-dependent Schrödinger equation. The calculations of the PES and dipole couplings are described in Sec. II B. Here we also analyze the effect of the pump pulse, in particular, the effect of population redistribution due to the resonant coupling in the case of a 800-nm pump laser. Our results are presented in Sec. III. To relate with earlier simulations, we first analyze in Sec. III A two-channel calculations with molecules aligned along the laser polarization. A more realistic, three-channel simulation with molecules aligned preferentially perpendicular to the laser polarization is presented in Sec. III B. Our most complete simulation is given in Sec. III C, in which population redistribution due to the resonant coupling is also taken into account. Here we also discuss the quantum beating between the nuclear wave packets on different PESs, $a\,^4\Pi_u$ and $b\,^4\Sigma_g^-$. Section III D is devoted to the analysis of high KER near 1.5 eV. In Sec. III E we show that by changing the laser wavelength, the probing of the nuclear wave packet can be made simple. This offers the possibility of extracting accurate parameters for the PES. The origin of the QB frequency near 48 THz is analyzed in Sec. III F. Our conclusions follow in Sec. IV.

Atomic units are used throughout the paper unless otherwise indicated.

II. THEORETICAL APPROACH

Our simulations for the effect of the probe pulse are based on solving the coupled-channel time-dependent Schrödinger equation (TDSE) in the Born-Oppenheimer (BO) representation. To simulate the effect of the pump pulse on the neutral O_2, we use the molecular Ammosov-Delone-Krainov (MO-ADK) tunneling ionization theory [18]. The structural parameters, including the PES and dipole couplings, were calculated using accurate quantum chemistry software. Here we briefly describe our method.

A. The coupled-channel time-dependent Schrödinger equation

The rotational period of O_2 is about 11.6 ps, which is much longer than the 10–15-fs laser pulse duration used in the experiments of De *et al.* [16]. It is therefore safe to assume that molecules do not rotate during the pulse. For the large pump-probe time delays up to about 2 ps used in the experiment, the molecular axis rotation after the pump can be somewhat non-negligible. Nevertheless, the main physics can already be understood for much shorter delays; we therefore assume that the molecular axis is fixed in space in all of the following treatment.

After expanding the total wave function in the BO electronic states, one obtains the coupled-channel time-dependent equation for the radial wave functions $\chi_i(R,t)$ as

$$i\frac{\partial}{\partial t}\begin{pmatrix}\chi_1\\ \chi_2\\ \vdots\end{pmatrix}=\begin{pmatrix}T_R+V_1 & \mathbf{E}(t)\cdot\mathbf{d}_{12} & \cdots\\ \mathbf{E}(t)\cdot\mathbf{d}_{12} & T_R+V_2 & \cdots\\ \vdots & \vdots & \ddots\end{pmatrix}\begin{pmatrix}\chi_1\\ \chi_2\\ \vdots\end{pmatrix}. \qquad (1)$$

Here $V_i(R)$ is the adiabatic BO potential of channel i, $\mathbf{d}_{ij}$ is the dipole coupling between channels i and j, $T_R = -1/2\mu\partial^2/\partial R^2$ is the nuclear kinetic energy operator, with μ being the nuclear reduced mass, and $\mathbf{E}(t)$ is the laser electric field vector. In this paper we used laser pulses with a Gaussian envelope

$$E(t) = E_0 e^{-2\ln(2)(t/\tau)^2}\cos(\omega t), \qquad (2)$$

where τ is the FWHM, E_0 is the laser electric field amplitude, and ω is the laser frequency.

We solve the coupled-channel equation (1) using the split-operator Crank-Nicolson method. We typically used radial spacing $\Delta R = 0.01$ a.u. and propagated up to $R_{\max} = 30$ a.u., with the time step $\Delta t = 3.5$ a.u. A mask function was also used to reduce the effect of a finite box size. All these parameters have been carefully checked to make sure the results are converged. In order to simulate KER spectra, we use the Fourier-transform (FT) technique as well as the virtual detector method [17,19]. We generally found the FT method to be superior. Therefore in this paper we report results only with the FT method.

B. Calculations of ${O_2}^+$ potential energy curves and the effect of the pump pulse

In Ref. [16], the measurement of time-delayed KER spectra was carried out on the O^+ ion signals from the velocity map imaging (VMI) spectrometer. To understand the dissociation dynamics imbedded in these data, one therefore needs to analyze the relevant potential energy curves of ${O_2}^+$ and the dipole couplings that enter Eq. (1).

In this work, the potential energy curves $V_i(R)$ and transition dipoles $\mathbf{d}_{ij}$ were calculated using MOLCAS [21] within the complete active space multiconfigurational self-consistent field method (CASSCF). We included 11 active electrons and eight molecular orbitals, that is, CASSCF(11,8), within the correlation-consistent polarized valence triple-ζ (cc-pVTZ)

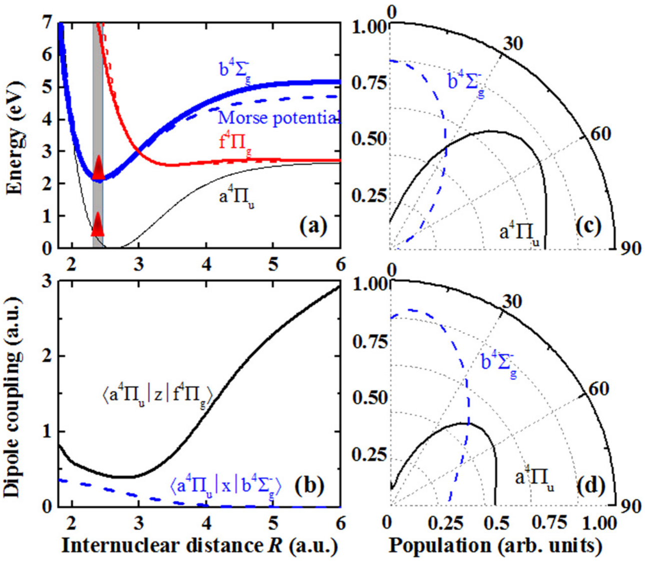

FIG. 1. (a) Calculated $O_2{}^+$ potential energy curves and (b) transition dipole couplings for main channels included in the simulations. The $f\,^4\Pi_g$ curve from Marian *et al.* [20] and the Morse potential for the $b\,^4\Sigma_g^-$ state are also shown as short and long dashed lines, respectively. (c) Angle-dependent rates for ionization from the ground-state O_2 to $O_2{}^+$ $a\,^4\Pi_u$ and $b\,^4\Sigma_g^-$ states, obtained from the MO-ADK at a laser intensity of 1.5×10^{14} W/cm^2. (d) Same as (c) but accounting for the "redistribution" due to the resonant coupling between $a\,^4\Pi_u$ and $b\,^4\Sigma_g^-$ states for a 15-fs laser pulse.

basis set. To avoid a root switching problem, we used the state-averaged CASSCF.

The results are shown in Figs. 1(a) and 1(b) for potential energy curves $V_i(R)$ and transition dipoles $\mathbf{d}_{ij}$, respectively, for the most relevant channels: $a\,^4\Pi_u$, $f\,^4\Pi_g$, and $b\,^4\Sigma_g^-$. The first two channels were originally identified as the main ones, leading to the measured KER signals in De *et al.* [16]. According to their interpretation, the experimental time-delayed KER spectra can be understood as the result of an initial creation of a vibrational wave packet in the $O_2{}^+$ $a\,^4\Pi_u$ state by the pump pulse, followed by its dissociation in the $f\,^4\Pi_g$ state after absorbing a photon from the probe pulse. This interpretation was later confirmed in more involved simulations by Magrakvelidze *et al.* [17], although the discrepancies with the experimental data remain. It should be noted that in these previous simulations the molecules were assumed to be perfectly aligned parallel to the laser polarization direction, whereas O^+ ions were detected experimentally in De *et al.* [16] at ±30° perpendicular to the laser polarization. As will be shown, our simulation, which accounts for realistic molecular partial alignment, reveals the important role of the $b\,^4\Sigma_g^-$ state. These three main channels were included in our simulation. Overall, our calculated potential energy curves and transition dipoles are in good agreement with Magrakvelidze *et al.* [17] and Marian *et al.* [20]. They also agree with more elaborate calculations based on the multireference configuration interaction (MRCI) by Zhang *et al.* [22], which compares very well with experimental data. We have found that inclusion of more channels in the simulation had unnoticeable effects on the low-energy KER results (below 1 eV) reported in this paper.

The effect of the pump pulse in the initial ionization of the ground-state neutral O_2 was modeled by the MO-ADK [18] theory. The ionization leading to the ground state of $O_2{}^+$ (i.e., $X\,^2\Pi_g$), by removing an electron from the highest occupied molecular orbital (HOMO), is irrelevant, since this deep bound state does not couple with the dissociating states. The angle-dependent ionization rates leading to $a\,^4\Pi_u$ and $b\,^4\Sigma_g^-$ states (by removing an electron from HOMO-1 and HOMO-2, respectively) are shown in Fig. 1(c) for the laser intensity of 1.5×10^{14} W/cm^2. We note that small variations in laser intensity lead to only minor changes in the ionization angular distribution. There is a significant population in the $b\,^4\Sigma_g^-$ state, especially at 0°. However, this state does not couple directly with the dissociating $f\,^4\Pi_g$ state due to the selection rules. Furthermore, since its coupling through the $a\,^4\Pi_u$ state is perpendicular, it is clearly irrelevant in the previous simulations [16,17] in which only molecules perfectly aligned parallel to the laser polarization were considered.

Based on the above discussion, we generally expect some influence on the O^+ signals due to the $b\,^4\Sigma_g^-$ state. In fact, its influence is greatly increased due to the strong resonant coupling between $b\,^4\Sigma_g^-$ and $a\,^4\Pi_u$ states by 800-nm lasers (with photon energy of 1.55 eV). In fact, the vertical ionization energies of these two states are 18.17 and 16.70 eV, respectively, resulting in the energy gap of 1.47 eV [23]. Below we analyze the influence of this coupling for the ionization distributions due to the pump pulse. We will address its effect on the dissociation dynamics due to the probe pulse in the next section.

To understand the influence of the $b\,^4\Sigma_g$–$a\,^4\Pi_u$ coupling during the pump pulse, we first note that the ionization rates shown in Fig. 1(c) were calculated within the quasistatic MO-ADK theory, i.e., without any consideration of the resonant coupling between the two states. In the case of a short pump pulse, it is reasonable to assume that tunneling ionization occurs near the peak of the pulse, which can be modeled properly by the MO-ADK theory. The vibrational distributions of the nuclear wave packet are modeled by the Franck-Condon (FC) factors. Our calculated FC factors, shown in Figs. 2(a) and 2(b) for $a\,^4\Pi_u$ and $b\,^4\Sigma_g^-$ states, respectively, are in good agreement with Gilmore *el al.* [24]. In order to account for the resonant coupling effect, these results were used to construct the initial nuclear wave packet for the coupled-channel equation (1), which was then propagated further until the end of the pump pulse, for each molecular alignment angle with respect to the laser's polarization. The results of this "redistribution" are shown in Fig. 1(d) for the case of a 15-fs pump pulse with an intensity of 1.5×10^{14} W/cm^2. Compared to the original MO-ADK results in Fig. 1(c), the population of the $b\,^4\Sigma_g^-$ state greatly increases at large angles near 90°, whereas the population of the $a\,^4\Pi_u$ state greatly decreases. This is understood as the strong population transfer from a more populated state ($a\,^4\Pi_u$) to a less populated state ($b\,^4\Sigma_g^-$) due to the perpendicular resonant transition discussed above.

For a more quantitative idea about the vibrational state "redistribution," we show their populations in Figs. 2(c) and 2(d) for $a\,^4\Pi_u$ and $b\,^4\Sigma_g^-$ states, respectively, for the molecular axis at $\theta = 80^\circ$ with respect to the laser polarization. We particularly note a significant suppression of $a\,^4\Pi_u$ populations

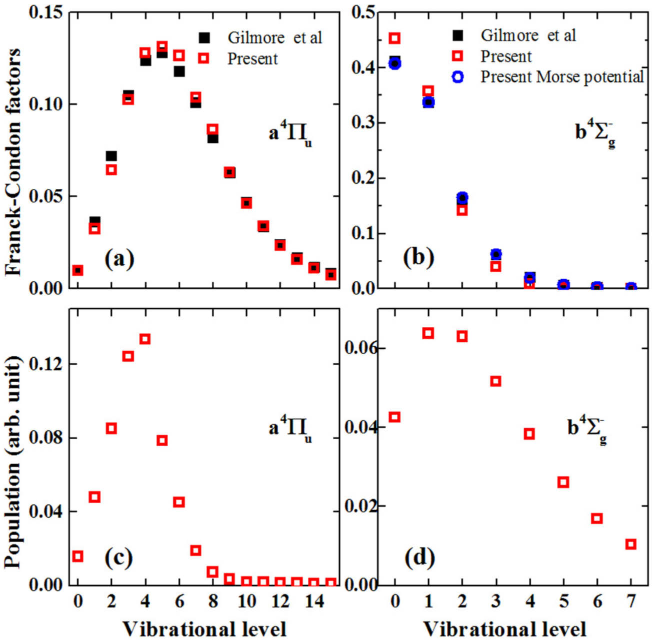

FIG. 2. The Franck-Condon factors for $a\,^4\Pi_u$ (a) and $b\,^4\Sigma_g^-$ (b) states. (c, d) Vibrational populations in $a\,^4\Pi_u$ and $b\,^4\Sigma_g^-$, respectively, after the population "redistribution" for a molecular axis at $\theta = 80°$ with respect to the laser polarization. The laser parameters are the same as for Fig. 1(d).

for large $v \gtrsim 10$, which are connected to the $f\,^4\Pi_g$ dissociating state through one photon absorption. On the other hand, there is a significant enhancement of $b\,^4\Sigma_g$ populations for $v \gtrsim 4$, which are connected to the same $f\,^4\Pi_g$ dissociating state through the $a\,^4\Pi_u$ channel. We will see in Sec. III C that this "redistribution" leads to strong modifications in the KER spectra. We further remark that a similar population redistribution was analyzed recently both experimentally and theoretically for N_2 by Yao *et al.* [25] in connection with the recently observed cavity-free lasing in ionized N_2 [26,27].

We have also checked the influence of the different shapes of the PECs on the KER yields. We found that the $f\,^4\Pi_g$ curve reported by Marian *et al.* [20] [see Fig. 1(a)] leads to an overall better agreement with experiments by De *et al.* [16] for the KER spectra below about 0.1 eV. A similar conclusion was also reached by Cörlin *et al.* [14] for their XUV pump–IR probe experiments. Since only low vibrational states are involved in the $b\,^4\Sigma_g^-$ channel, we also used a Morse potential for this state, in addition to the calculated potential from MOLCAS. The parameters used for the Morse potential were taken from Zhang *et al.* [22].

III. RESULTS

A. Two-channel calculations with molecules aligned parallel to laser polarization

In order to compare with calculations reported in Refs. [16,17], in this section we discuss the calculations with molecules perfectly aligned parallel to the laser's polarization, as it was assumed in those early simulations. In this case, three-channel (with $a\,^4\Pi_u$, $b\,^4\Sigma_g^-$, and $f\,^4\Pi_g$ states) calculation is identical to two-channel calculation (with $a\,^4\Pi_u$ and $f\,^4\Pi_g$ states), since the $b\,^4\Sigma_g^-$ state does not couple with the $a\,^4\Pi_u$ and $f\,^4\Pi_g$ states. We further assume that the vibrational distributions in the $a\,^4\Pi_u$ and $b\,^4\Sigma_g^-$ states after the pump pulse are given by the FC factors, shown in Figs. 2(a) and 2(b), as it was used in Refs. [16,17].

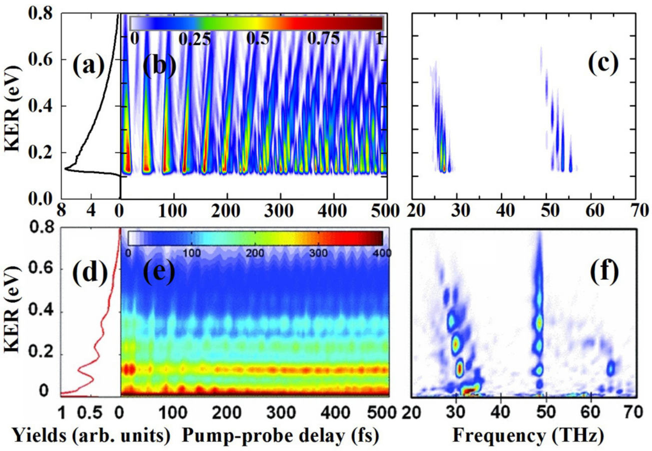

FIG. 3. Two-channel calculation for the KER spectrum (a), its pump-probe time-delay dependence (b), and the QB spectrum (c) with a 10-fs probe laser pulse with an intensity of 3×10^{14} W/cm^2. The molecule is assumed to be perfectly aligned along the laser polarization. (d, e, f) Same as (a)–(c), but from the experimental measurements by De *et al.* [16]. (d), (e), and (f) are adopted from Magrakvelidze *et al.* [17], copyrighted by the American Physical Society.

Our calculated KER spectrum vs time delay for a 10-fs laser pulse with an intensity of 3×10^{14} W/cm^2, shown in Fig. 3(b), is practically identical to those from early simulations [16,17]. Compared to the experimental data, shown in Fig. 3(e), there is clear overall agreement. In particular, the oscillatory structure with respect to time delay and the progressive tilt in the KER with increased delays can be seen in both experiment and theory. The first feature can be understood as originating from the nuclear-wave-packet motion in the $a\,^4\Pi_u$ potential, mapped into the dissociating $f\,^4\Pi_g$ potential after absorbing a photon near $R = 3.2$ a.u. The second feature is caused by the fact that the vibrational period of a higher vibrational state in the $a\,^4\Pi_u$ (leading to higher KER) potential is larger than that of a lower vibrational state (leading to smaller KER). The positive tilt in time delay corresponds to the negative slope in the QB spectrum, seen in both theory and experiment near 27 and 32 THz, respectively, in Figs. 3(c) and 3(f).

However, a closer examination reveals two important discrepancies between theory and experiment. (i) The theoretical KER spectrum [Figs. 3(a) and 3(b)] as a function of energy shows no structure, whereas the experimental spectrum [Figs. 3(d) and 3(e)] has a strong energy-dependent structure. To improve the agreement with experiments, Magrakvelidze *et al.* [17] added a long (100-fs) pedestal pulse to the probe pulse. Nevertheless, only a very weak energy-dependent structure was obtained, still in disagreement with De *et al.* [16]. (ii) The theoretical QB frequency is strongly peaked near 27 THz, whereas it is near 32 THz in experiment. One might wonder if this "small" discrepancy is due to the inaccuracy of the theoretical $a\,^4\Pi_u$ potential curve. In fact, simulation results shown in Fig. 3 were obtained by using the $a\,^4\Pi_u$ potential curve from Magrakvelidze *et al.* [17]. If our calculated $a\,^4\Pi_u$ potential curve is used, the QB frequency shifts to about 25 THz. Furthermore, a high-quality $a\,^4\Pi_u$ potential curve from Zhang *et al.* [22] also leads to the QB frequency near 24 THz between $v = 10$ and $v = 11$, which is in good agreement with the photoelectron data by Song *et al.* [28]. Although for vibrational states near $v = 0$ the QB frequency increases to near 30 THz, these low vibrational states (with $v \leqslant 10$) do not connect to dissociating $f\,^4\Pi_g$ states by a 1.55-eV photon. This discrepancy was noticed earlier by De *et al.* [16] (see their Fig. 7 and related discussion). The discrepancy becomes even larger for the weaker QB frequency with $\Delta v = 2$, which occurs near 55 THz in our simulation, whereas in the experiment it is near 65 THz [see Figs. 3(c) and 3(f), respectively]. Note that the strong vertical line near 48 THz in the experimental QB spectrum has a different origin, which will be analyzed in Sec. III F.

We further remark that theoretical KER yields practically vanish for energy below about 0.1 eV, in strong contrast to the experimental data. We found that the presence of the weak potential barrier near $R = 4.5$ a.u. in our theoretical $f\,^4\Pi_g$ curve gives rise to a resonance which eventually dissociates. Account for this resonance requires a long propagation time, which is inefficient for computational purposes. To avoid this complication, in the following we use the theoretical $f\,^4\Pi_g$ curve from Marian *et al.* [20]. It was also noticed earlier by Cörlin *et al.* [14] that the Marian *et al.* curve led to an overall better agreement with their experimental data at very low KERs. As can be seen in Fig. 1(a), the two theoretical curves are nearly indistinguishable.

B. Three-channel calculations without population redistribution

In this paper we show that the discrepancies, discussed in the above subsection, can be resolved if one takes into account the following in the simulation: (i) the molecules that are detected in experiment are aligned close to 90° with respect to the laser polarization; (ii) the strong influence of the $b\,^4\Sigma_g^-$ state on the KER spectra; and finally, (iii) the population "redistribution" in $a\,^4\Pi_u$ and $b\,^4\Sigma_g^-$ states due to the resonant coupling between these two states by the 800-nm laser pulse, as discussed in Sec. II B. In this section, we take into account the first two items. The last one will be discussed in the next section.

Our three-channel calculations (with $a\,^4\Pi_u$, $b\,^4\Sigma_g^-$, and $f\,^4\Pi_g$ states) are shown in Fig. 4(b) for the KER spectrum versus time delay for a 15-fs laser pulse with an intensity of 1×10^{14} W/cm^2. Here the results have been averaged over the experimental detection range of 90° ± 30° for the molecular axis with respect to the laser polarization. Here, for simplicity in the simulation, we omit the region with overlapping pump and probe pulses. In contrast to the results shown in Fig. 3(b) and early simulation by Magrakvelidze *et al.* [17], the appearance of the energy-dependent structure is rather striking. This can also be easily seen in the data integrated over all time delays, shown in Fig. 4(a). These oscillatory structures resemble very closely the experimental data of De *et al.* [16] in Figs. 3(d) and 3(e). Despite this improvement, the main QB signals (with $\Delta v = 1$) still remain close to about 25 THz [see Fig. 4(c)], reflecting the fact that the main contribution to dissociation comes from the vibrational wave packet in the $a\,^4\Pi_u$ state. There is no clear signature of the contribution from the wave packet in the $b\,^4\Sigma_g^-$ state. This can be understood as due to the small population in the $b\,^4\Sigma_g^-$ state at large angles near 90° [see Fig. 1(c)], especially for $v \geqslant 4$ [see Fig. 2(b)], which are above the first dissociation limit. In fact, our two-channel calculations lead to nearly the same results, except for overall yields, which were increased by about 20%. Here, the smaller KER yields in the three-channel case, as compared to the two-channel case, can be attributed to the "leaking" of the $a\,^4\Pi_u$ population to the $b\,^4\Sigma_g^-$ state near 90°. We will see in the next section that the situation changes drastically when the population "redistribution" is taken into account.

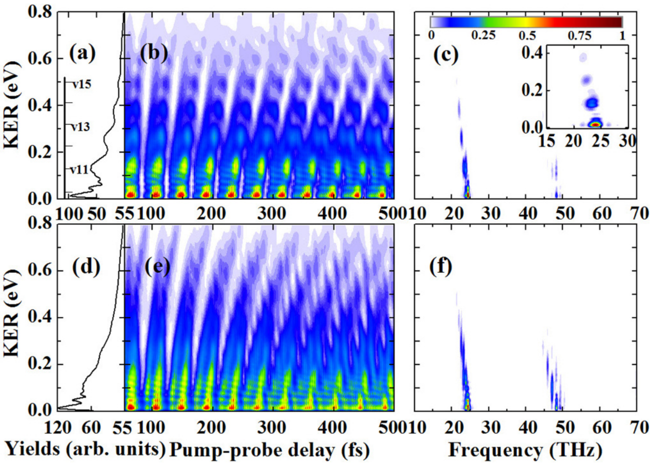

FIG. 4. Three-channel calculation without population "redistribution" for the KER spectrum (a), its pump-probe time-delay dependence (b), and the QB spectrum (c) with a 15-fs probe laser pulse with an intensity of 1×10^{14} W/cm^2. The results have been averaged over O^+ detection angles near 90° with respect to the laser polarization. The vertical scale in (a) marks the vibrational energies in the $a\,^4\Pi_u$ state after absorbing one photon. (d, e, f) Same as (a), (b), and (c) but for a laser intensity of 3×10^{14} W/cm^2. The inset in (c) shows a zoom-in of the QB spectrum obtained with a maximum time delay of 700 fs.

Note that the QB spectrum was obtained with the delay time up to 2 ps (as used in the experiment by De *et al.* [16]). As the rotational period of O_2 is 11.6 ps, the molecular rotation cannot be totally neglected. We therefore also performed QB analysis with the maximum time delay of 700 fs. The result is shown as the inset in Fig. 4(c). The KER peaks look broader and closely mimics the shape of experimental KER peaks.

The energy-dependent structure gets much weaker when the laser intensity increases to 3×10^{14} W/cm^2 [see Figs. 4(d), 4(c) and 4(f)]. To better understand this effect, we show in Fig. 5(a) the KER yields at several fixed molecular axis angles at a laser intensity of 1×10^{14} W/cm^2. The KER peaks for different angles occur nearly at the same energies, resulting in the total (angle-integrated) strong oscillation in the KER yields vs energy, as seen in Fig. 4(a). The KER peaks can be assigned to specific vibrational states of $a\,^4\Pi_u$, from $v = 10$ on up. As the laser intensity increases to 3×10^{14} W/cm^2, the

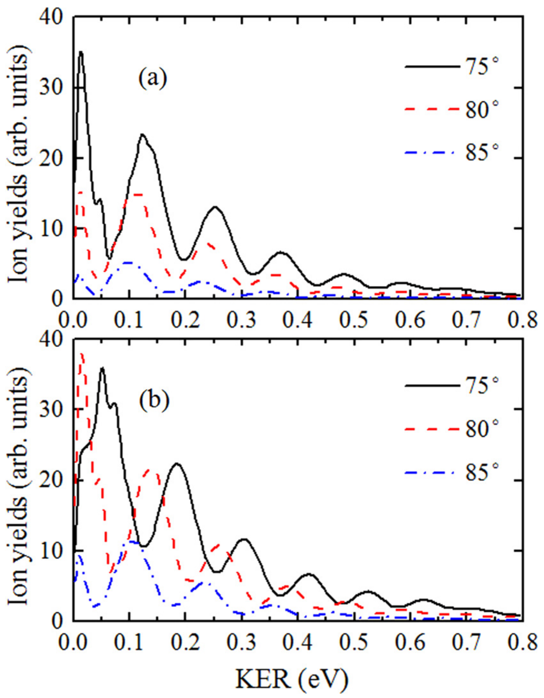

FIG. 5. (a) KER spectra for fixed angles of $\theta = 75^\circ$, 80°, and 85° at a laser intensity of 1×10^{14} W/cm^2. The three-channel calculations were carried out without the population redistribution. (b) Same as (a) but for a laser intensity of 3×10^{14} W/cm^2.

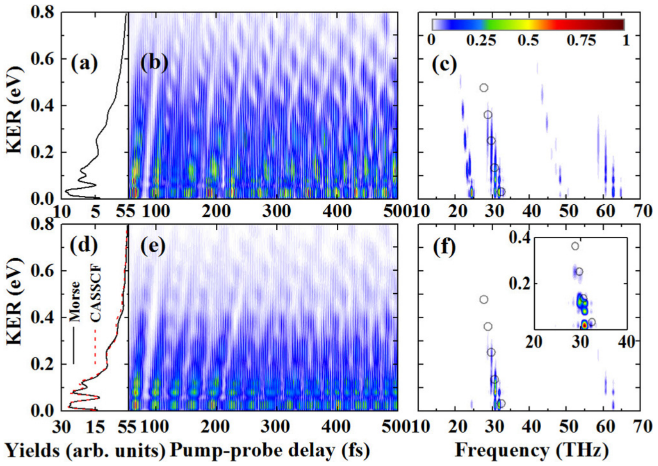

FIG. 6. Three-channel calculation with population "redistribution" for KER spectrum (a), its pump-probe time-delay dependence (b), and the QB spectrum (c) with a 10-fs probe laser pulse with an intensity of 1×10^{14} W/cm^2. The results have been averaged over the detection angles near 90° with respect to the laser polarization. (d, e, f) Same as (a), (b), and (c), but for a 15-fs laser pulse. The black empty circles in (c) and (f) mark the experimental KER peaks from De *et al.* [16]. In (d) both KER spectra using Morse and current CASSCF potential curves for the $b\,^4\Sigma_g^-$ state are shown. The inset in (f) shows the zoom-in of the QB spectrum obtained with the maximum time delay of 700 fs at $\theta = 80^\circ$.

KER peaks shift significantly with the alignment angles [see Fig. 5(b)]. This results in a rather smooth KER spectrum as seen in Fig. 4(d). The shifts in the KER peaks can be associated with the Stark shifts in the vibrational levels, which can generally be understood as due to the deformation of the potential energy curves in the intense laser field [29]. In our case, the shifts are especially strong since large v ($v \geqslant 10$) are involved. For completeness we note that the two-channel calculations at 0° also show a strong energy-dependent oscillatory structure at very low probe laser intensities, typically below about 1×10^{13} W/cm^2.

C. Three-channel calculations with population redistribution

We now present our most complete simulations that further extend the calculations of the previous section to include the population redistribution. As discussed in Sec. II B, description of tunneling ionization to the ionic $a\,^4\Pi_u$ and $b\,^4\Sigma_g^-$ states by the quasistatic MO-ADK theory is not adequate at 800-nm wavelength due to the strong resonant coupling between these two states. Our simulated KER spectra are shown in the upper (or lower) panel of Fig. 6 for a 10-fs (or 15-fs) probe pulse.

Let us first analyze the case of a 10-fs pulse. The overall structures of the KER spectrum and its time-delay dependence appear to be still similar to those of Fig. 4. However, in contrast to Fig. 4(c), the QB spectrum in Fig. 6(c) now shows additional peaks near 32 and 64 THz, which are the signature of the vibrational wave-packet motion associated with the $b\,^4\Sigma_g^-$ state, for $\Delta v = 1$ and $\Delta v = 2$, respectively, with $v \geqslant 4$. These are exactly the positions of the experimental KER peaks, shown in black circles in the figure for the group near 32 THz. Clearly, the increased KER yields associated with the $b\,^4\Sigma_g^-$ state are due to the increased populations in the $b\,^4\Sigma_g^-$ state, especially for $v \geqslant 4$ for large angles near $\theta = 90^\circ$, as compared to the prediction from the standard MO-ADK theory [cf. Figs. 1(d) and 2(d) with Figs. 1(c) and 2(b)].

The KER yields associated with the $b\,^4\Sigma_g^-$ state can be further increased if the probe pulse is longer. This is illustrated in the lower panel of Fig. 6 for a 15-fs pulse. Here the signals associated with the $b\,^4\Sigma_g^-$ state (near 32 and 64 THz) are so dominant that the signals associated with the $a\,^4\Pi_u$ state become practically invisible in the figure. The increased KER signals associated with the $b\,^4\Sigma_g^-$ state for the longer pulse can be understood, as this state couples with the dissociating $f\,^4\Pi_g$ state only through $a\,^4\Pi_u$ state. It requires some time for the portion of the wave packet, transferred originally from the $b\,^4\Sigma_g^-$ state to the $a\,^4\Pi_u$ state during the probe pulse, to propagate to near $R = 3.5$ a.u., where it can be efficiently promoted to the $f\,^4\Pi_g$ state. To reduce the influence of the molecular axis rotation, we also performed the QB analysis with a maximum time delay of 700 fs. The result shown in the inset of Fig. 6(f) also resembles quite closely the experimental QB data near 32 THz.

All the results presented here have been averaged over the experimental detection range of 90° ± 30° with respect to laser polarization. As noted in the previous section, the energy-dependent structure is generally more pronounced for a fixed molecular alignment angle. We also remark that for the KER yields below 0.8 eV, the calculations using the CASSCF potential curve for the $b\,^4\Sigma_g^-$ state are nearly identical to those with the Morse model potential, as shown in Fig. 6(d).

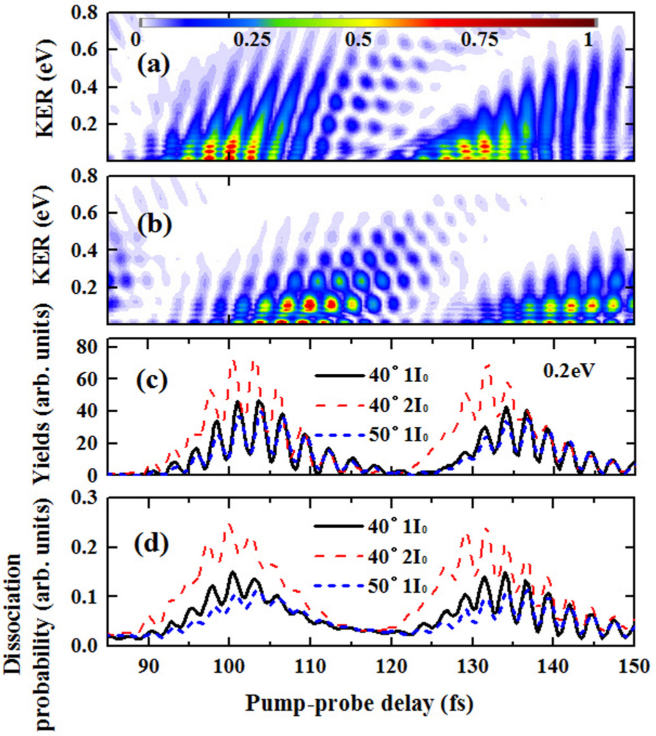

FIG. 7. Zoom-in of the KER spectrum for a pump-probe time delay of [85 − 150] fs for a fixed molecular axis at (a) $\theta = 40^\circ$ and (b) 80°. (c) The ion yields versus time delay at KER near 0.2 eV for different molecular alignment angles and laser intensities (as indicated in the labels). Here $I_0 = 1 \times 10^{14}$ W/cm^2. (d) Same as (c) but for the total dissociation yields.

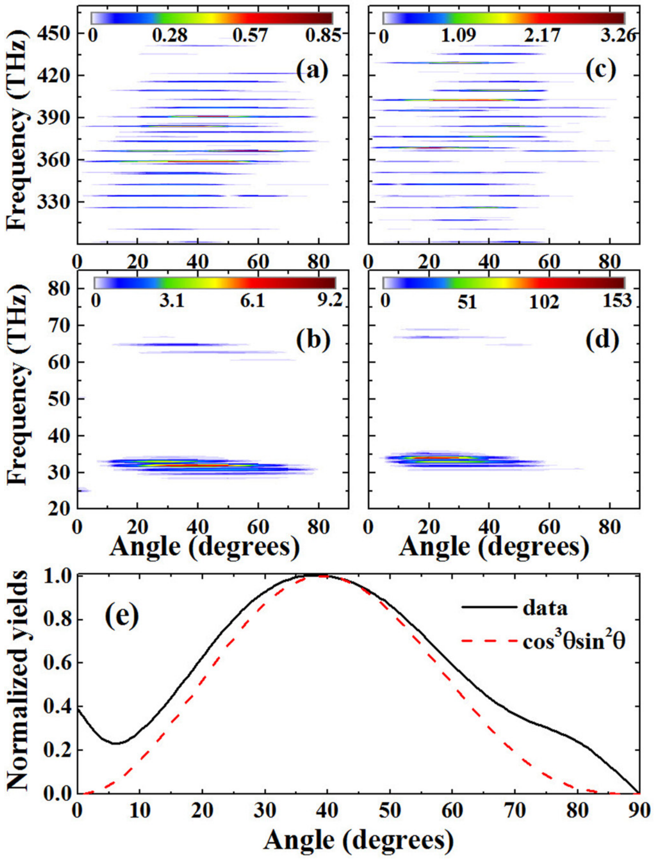

FIG. 8. (a, b) Dissociation signals vs QB frequency and molecular axis angle (i.e., ion detection direction with respect to the laser polarization) at a probe laser intensity of 1×10^{14} W/cm^2, for high and low QB frequencies, respectively. (c, d) Same as (a) and (b) but for a probe laser intensity of 3×10^{14} W/cm^2. (e) Normalized total dissociation yields vs molecular axis angle. The simple analytical model is shown as the dashed line. See text for more details.

The good agreement with experiment discussed above suggests that the observed QB frequencies near 32 THz are associated with the wave packet on the $b\,^4\Sigma_g^-$ curve rather than on the $a\,^4\Pi_u$ curve, as proposed in Refs. [16,17]. We further note that the measured revival time was 1200 fs (as cited in Ref. [17]), whereas the spectroscopic revival time is 1605 and 976 fs for $a\,^4\Pi_u$ and $b\,^4\Sigma_g^-$, respectively [30]. Clearly, further theoretical studies as well as improved measurements of the revival time are desirable to fully resolve this remaining discrepancy.

A closer inspection of the time-delay KER spectrum in Fig. 6(e) reveals fine oscillations with a period of about 3 fs. Figures 7(a) and 7(b) show the zoom-in for the pump-probe time delay of [85–150] fs for a fixed molecular axis at $\theta = 40^\circ$ and 80°, respectively, with respect to the laser polarization. Although the KER distribution pattern depends on the molecular alignment, the fine-structure peak positions are relatively stable with respect to laser intensity and the molecular alignment, as shown in Fig. 7(c) for a fixed KER of 0.2 eV. Combined with the strong contrast in the modulation peaks, this result suggests that these oscillations can, in principle, be observed experimentally. We further note that for the total dissociation signals (integrated over all energies) shown in Fig. 7(d), the oscillations at different laser intensities and molecular alignments are still in phase, although the contrast is weaker. These oscillations are associated with the QB peaks near 375 ± 75 THz (or 1.55 ± 0.3 eV) [see Figs. 8(a) and 8(c)]. Here, the QB signals (integrated over all KER) are plotted as functions of alignment angle and QB frequency for probe laser intensities of 1×10^{14} and 3×10^{14} W/cm^2, respectively. The origin of these QB can be understood as the beating of the vibrational states belonging to different electronic states, $a\,^4\Pi_u$ and $b\,^4\Sigma_g^-$ in our case. The bandwidth of ±75 THz simply reflects the bandwidth of the probe laser. This "interchannel" beating is in contrast to the QB near 25 and 32 THz, where the beating occurs as the result of interference of the signals originating from two different v (with $\Delta v = 1$) within the same electronic state, $a\,^4\Pi_u$ and $b\,^4\Sigma_g^-$, respectively. Note that the beating by the nuclear wave packets on the different electronic states is only possible as long as these wave packets were created coherently, as in De *et al.* [16]. For example, it was not the case in the experiment with ion-beam targets by Zohrabi *et al.* [31].

The angle dependence of the dissociation yields are shown in Figs. 8(a) and 8(b) for high and low QB frequencies, respectively, at a probe laser intensity of 1×10^{14} W/cm^2. The yields are generally peaked at some intermediate angles near 45°. At a higher laser intensity of 3×10^{14} W/cm^2, shown in Figs. 8(c) and 8(d), the angular distributions change somewhat but the QB frequencies remain the same as for the lower-intensity case. This reflects the fact that the QB frequencies are the properties of the laser-free PESs. In principle, the QB frequencies can be assigned to a specific beating. This will be further illustrated in Sec. III E for the low-QB region. A more involved analysis of the high-QB region will be presented elsewhere. The total (normalized) dissociation yields vs molecular alignment angle are shown in Fig. 8(e). They compare quite well with a simple model, based on angular dependence of the dipole couplings between the involving states and the approximation of the $b\,^4\Sigma_g^-$ population as $\cos\theta$. These results suggest that the measurements by De *et al.* [16] near 90° were not optimal for the total yields. The choice of 90° detection by De *et al.* was caused by the use of the VMI setup. This limitation can be lifted by using the cold-target recoil-ion momentum spectroscopy (COLTRIMS) setup as was done in Cörlin *et al.* [14].

Note that the present results are different from those of Cörlin *et al.* [14] for the case of XUV pump–IR probe experiments, where the peaks were found along the laser polarization direction. We further remark that in Cörlin *et al.* there is no population redistribution due to the XUV pump pulse so that the low-energy KER yields originate predominantly from the vibrational wave packet in the $a\,^4\Pi_u$ state, leading to the observed QB frequency of about 25 THz (or 0.1 eV).

D. On the origin of the broad peak near 1.5 eV in the KER spectra

In the experiment by De *et al.* [16], a rather strong and broad peak near 1.5 eV in the KER spectrum was observed. A strong oscillation in the pump-probe time delay was also seen for this peak. The experimental QB spectrum for this peak is in the range of 30–35 THz. It is therefore quite possible that this peak has the same mechanism as the low-KER peaks but with an additional photon absorbed, as speculated in Ref. [16]. However, our three-channel calculations with or without population redistribution for a large range of laser intensities show only a very weak broad peak near 1.5 eV, in disagreement with experiment. We found that this peak can be significantly enhanced (typically by an order of magnitude) by including an additional $^4\Sigma_u^+$ state [see Fig. 9(c)]. A typical KER spectrum up to 2 eV is shown in Figs. 9(a) and 9(b) for a laser intensity of 1×10^{14} W/cm^2 and the molecular axis angle of $\theta = 85°$. Note that the signals above 1.3 eV have been multiplied by a factor of 5 for clarity. The peak near 1.5 eV is much weaker than experimental data from De *et al.* [16]. We further found that this relatively fair agreement with experiment does not improve much by increasing the laser intensity or by including a few additional channels.

These results suggest that another mechanism might play an important role here. One possible mechanism could be predissociation, in particular, predissociation of the $B\,^2\Sigma_g^-$ state [see Fig. 9(c)]. Similar to $b\,^4\Sigma_g^-$, this state can be populated by removing an electron from the HOMO-2 of O_2 by the pump pulse. In fact, these two states differ only by the spin coupling. As reported by Lu *et al.* [32], this state predissociates very efficiently to the first dissociation limit, resulting in a KER near 1.6 eV. In the probe laser pulse, this state can couple with the $3\,^2\Pi_u$ state, thereby altering its population. This might lead to the expected oscillation in the KER yields with the period of the vibrational wave packet on the $B\,^2\Sigma_g^-$ curve. Note that the shape of the $B\,^2\Sigma_g^-$ potential energy curve is quite similar to that of $b\,^4\Sigma_g$, such that they have quite similar vibrational periods. This results in the QB frequencies near 30–35 THz, as seen in the experiment by De *et al.* [16]. If this speculation is valid, the position of the peak near 1.5 eV should be relatively stable with the probe laser wavelength. Clearly, further experiments are desirable in order to shed light into this problem. We also remark that the smallness of the recently measured β asymmetry parameter by Tang *et al.* [33] strongly suggests that the lifetime of the $B\,^2\Sigma_g^-$ state is larger than the rotational period. However, an earlier measurement by Evans *et al.* [34] suggests a lifetime of only about 0.4–2 ps, whereas Richard-Viard *et al.* [35] found a rather long lifetime of about 70 ns.

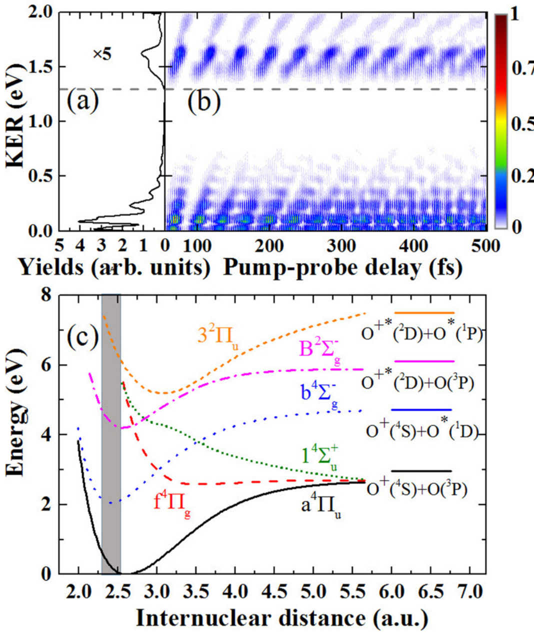

FIG. 9. Integrated KER spectrum (a) and its pump-probe time-delay dependence (b) up to 2 eV for a probe laser intensity of 1×10^{14} W/cm^2 at the molecular alignment angle $\theta = 85°$. An additional state $^4\Sigma_u^+$ was included in the four-channel calculation. Note that the signals above 1.3 eV (indicated by the horizontal dashed line) have been rescaled up by a factor of 5 for clarity. (c) Schematic of the potential curves most relevant to the KER peak near 1.5 eV, together with their dissociation limits.

E. Probing the potential energy curves with different laser wavelengths: 400-nm case

All the above discussion so far might give a false impression that probing a potential energy curve by following a nuclear wave packet is difficult, even for a simple target such as O_2. In this section we show that this is not necessarily the case. Here we illustrate this point on one simple case with a different laser wavelength of 400 nm for both pump and probe. This wavelength is chosen simply to avoid the complication due to the resonant coupling between $a\,^4\Pi_u$ and $b\,^4\Sigma_g^-$ states. In that

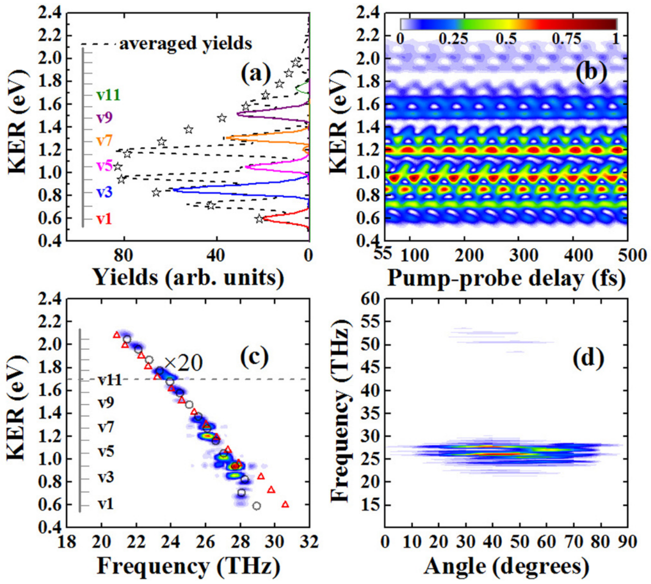

FIG. 10. Integrated KER spectrum (a), its pump-probe time-delay dependence (b), and QB spectrum (c) with 400-nm laser pulses. A 25-fs probe laser pulse with an intensity of 1×10^{14} W/cm^2 at the molecular alignment angle $\theta = 60^\circ$ was used. Black stars in (a) denote the FC factors (in arbitrary units) for vibrational populations in the $O_2{}^+$ $a\,^4\Pi_u$ state after the pump pulse. In (c) the QB signals above 1.7 eV (indicated by the horizontal dashed line) have been multiplied by a factor of 20 for visual clarity. Black circles in (c) are the theoretical estimates for the QB peaks using the CASSCF potential curve for the $a\,^4\Pi_u$ state, while the red triangles indicate the curve from Zhang *et al.* [22]. (d) Dissociation yields vs QB frequency and molecular axis angle θ.

case, only the wave packet on $a\,^4\Pi_u$ is "probed" by the probe pulse.

Our calculated KER spectra are shown in Figs. 10(a)–10(c) for a molecule axis at $\theta = 60^\circ$. Experimentally, it means that the O^+ ion detector is located at 60° with respect to the laser polarization. A 25-fs, 400-nm laser pulse with an intensity of 1×10^{14} W/cm^2 was used. A very strong energy- and delay-dependent spectrum can be seen in Fig. 10(b). The integrated KER spectrum [dotted line in Fig. 10(a)] shows quite distinct peaks which can be associated with different vibrational levels, as indicated by the vertical scale. For comparison, we also simulated the KER yields from single vibrational states with the population taken as the FC factors. For clarity, we show in Fig. 10(a) only the results from single states with odd v as the solid lines. They agree very well with the simulation using the actual nuclear wave packet (dotted line). Here all the peaks associated with $v = 1-12$ are visible. Recall that for an 800-nm laser, the lowest state one can possibly access is $v = 10$. Clearly, by changing the laser wavelength one can explore different regions of the potential curve. We note that the KER yields can be suppressed in certain states, as seen in Fig. 10(a) for $v = 5$. This suppression has been discussed earlier in terms of suppressed dipole couplings, see Ref. [31].

The resulting QB spectrum is shown in Fig. 10(c). The positions of the KER peaks agree quite well with the theoretical estimates (black circles) from our calculated $a\,^4\Pi_u$ potential curve, which was used in the actual simulation for the coupled-channel equation (1). Although the KER peaks are slightly shifted from the estimates for large v, they are still in line with the estimates. For comparison we also show the theoretical estimates based on the curve from Zhang *et al.* [22] (red triangles). Differences can be seen for energies below 0.9 eV (or $v \leqslant 3$). We found that if the Zhang *et al.* curve were used in the TDSE equation (1), the simulated results would agree better with the red triangles. This result implies that properties of the PES can be examined to high accuracies in real pump-probe experiments by following the nuclear motions. For completeness, we show in Fig. 10(d) the angle-dependent dissociation yields vs QB frequency. The yields again peak at an intermediate angle near 45°.

F. On the origin of the quantum beat frequency near 48 THz

The experimental QB spectrum in Fig. 3(f) shows a strong group near 48 THz which appears to be vertical instead of having a negative slope as the main group near 32 THz. This suggests a different origin for this group. Since the experimental probe pulse is as intense as the pump pulse, $O_2{}^+$ (say, in $a\,^4\Pi_u$) can be generated by the probe pulse directly from the neutral O_2 molecules that survive after the pump pulse. The resulting $O_2{}^+$ then can absorb one photon from the same pulse to the $f\,^4\Pi_g$ state, which dissociates into $O^+ + O$. Clearly, the probe pulse needs to be sufficiently long so that the newly created wave packet in the $O_2{}^+$ $a\,^4\Pi_u$ state has time to travel to the resonant excitation distance near $R = 3.2$ a.u. Since the dipole coupling is quite strong at large R [see Fig. 1(b)], a rather weak field near the trailing edge of the Gaussian pulse might suffice. As noted by De *et al.* [16], the QB frequency of 48 THz is close to the beating frequency between $v = 0$ and $v = 1$ of neutral O_2. The low-v vibrational wave packet in neutral O_2 could be created by the pump pulse through either a "Lochfrass" process [36,37] or Raman excitation, or the combination of both.

The result of our two-channel simulation (with $a\,^4\Pi_u$ and $f\,^4\Pi_g$) for the QB spectrum from neutral O_2 is shown in Fig. 11(a). The 25-fs laser pulse with intensity of 1.5 W/cm^2 was used. A reasonably good agreement with experiment can be seen. However, the most dominant KER peak is near 0.1 eV in the simulation. A better agreement with experiment was obtained by our three-channel calculation (with the addition of a $b\,^4\Sigma_g^-$ state), as shown in Fig. 11(b). Here the KER peaks near 0.4 eV are the most dominant. By reducing the pulse duration to 15 fs, the distinct KER peaks disappear. Instead, one obtains only a smooth line near 48 THz. This result suggests that the actual pulse duration in De *et al.* [16] might be somewhat longer than the original estimate (10–15 fs).

A few words are in order about the nature of the vertical line near 48 THz. As we have shown earlier, the negative slope in the QB spectrum near 32 THz reflects the fact that high vibrational states (which are connected to higher KER) in the nuclear wave packet in $O_2{}^+$ have a longer vibrational period than the lower vibrational states (which are connected to lower KER). In contrast, each KER peak near 48 THz, originating from the wave-packet motion in the ground electronic state of O_2, is not correlated with a specific vibrational state of O_2. Instead, in our case, all the peaks are correlated with the same

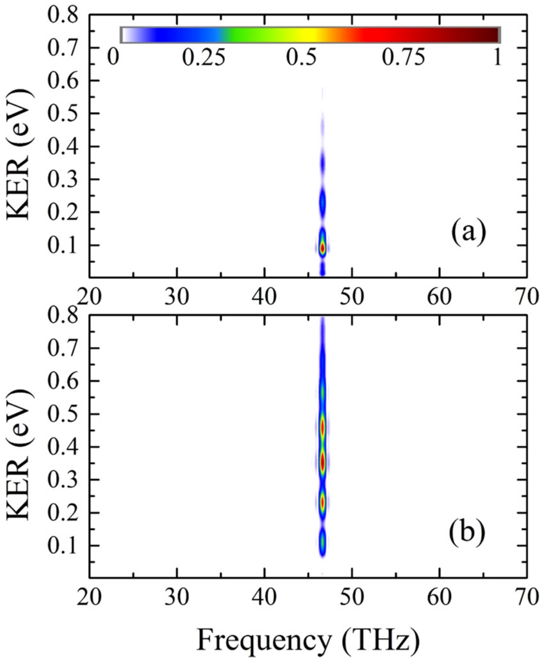

FIG. 11. QB spectrum for the scenario when both ionization from neutral O_2 and subsequent dissociation occur during the probe pulse. The results from two-channel and three-channel calculations are shown in (a) and (b), respectively.

beating between $v = 0$ and 1, which results in a vertical line in the QB spectrum near 48 THz.

IV. SUMMARY

We have performed extensive theoretical simulations in order to understand the IR pump–IR probe experiment on O_2 by De *et al.* [16]. Two important discrepancies between the experiment and early theoretical calculations reported in Refs. [16,17] in the presence of an energy-dependent structure and the location of the quantum beat frequencies are now resolved. We have identified the important role of the ${O_2}^+$ $b\,^4\Sigma_g^-$ state which is resonantly coupled to the $a\,^4\Pi_u$ state by the 800-nm laser. Although the $b\,^4\Sigma_g^-$ state is only weakly populated near $\theta = 90^\circ$ through direct tunneling ionization by the pump pulse, the near-resonant coupling draws populations that further contribute to the dissociation initiated by the probe pulse.

Our simulations reveal that multiple vibrational wave packets on different potential energy surfaces can be strongly coupled whenever resonant or near-resonant conditions are satisfied. In such situations, as in De *et al.*, the detailed vibrational structure can still be understood, but careful simulations and analysis are needed. To simplify the probing of nuclear dynamics, it is advisable to choose laser wavelengths that would not populate new channels resonantly. In such cases, the KER distribution vs the time delay and QB spectra can be used to extract accurate properties of the potential curves, as exemplified by the simulation using 400-nm laser pulses. Our results clearly illustrate how accurate identification of the main channels involved in typical pump-probe experiments can be achieved by extensive comparison between theoretical calculations with experimental data. Such analysis is difficult to implement with pure brute-force solutions of the many-electron molecules in strong fields such as the time-dependent Schrödinger equation or the popular time-dependent density functional theory (TDDFT).

ACKNOWLEDGMENTS

We thank Prof. Uwe Thumm for fruitful discussion. This work was supported by the Chemical Sciences, Geosciences and Biosciences Division, Office of Basic Energy Sciences, Office of Science, U.S. Department of Energy under Grant No. DE-FG02-86ER13491. S.X. was supported by the China Scholarship Council for two-year study at Kansas State University.

---

[1] A. H. Zewail, Science **242**, 1645 (1988).
[2] A. H. Zewail, J. Phys. Chem. A **104**, 5660 (2000).
[3] T. Ergler, A. Rudenko, B. Feuerstein, K. Zrost, C. D. Schröter, R. Moshammer, and J. Ullrich, Phys. Rev. Lett. **97**, 193001 (2006).
[4] A. S. Alnaser, B. Ulrich, X. M. Tong, I. V. Litvinyuk, C. M. Maharjan, P. Ranitovic, T. Osipov, R. Ali, S. Ghimire, Z. Chang, C. D. Lin, and C. L. Cocke, Phys. Rev. A **72**, 030702 (2005).
[5] M. Meckel, D. Comtois, D. Zeidler, A. Staudte, D. Pavičić, H. C. Bandulet, H. Pépin, J. C. Kieffer, R. Dörner, D. M. Villeneuve, and P. B. Corkum, Science **320**, 1478 (2008).
[6] M. Lein, J. Phys. B **40**, R135 (2007).
[7] C. D. Lin, A.-T. Le, Z. Chen, T. Morishita, and R. Lucchese, J. Phys. B **43**, 122001 (2010).
[8] C. I. Blaga, J. Xu, A. D. DiChiara, E. Sistrunk, K. Zhang, P. Agostini, T. A. Miller, L. F. DiMauro, and C. D. Lin, Nature (London) **483**, 194 (2012).
[9] M. Pullen, B. Wolter, A. T. Le, M. Baudisch, M. Hemmer, A. Senftleben, C. D. Schröter, J. Ullrich, R. Moshammer, C. D. Lin, and J. Biegert, Nat. Commun. **6**, 7262 (2015).
[10] W. Li, X. Zhou, R. Lock, S. Patchkovskii, A. Stolow, H. C. Kapteyn, and M. M. Murnane, Science **322**, 1207 (2008).
[11] H. Worner, J. Bertrand, D. Kartashov, P. Corkum, and D. Villeneuve, Nature (London) **466**, 604 (2010).
[12] H. J. Wörner, J. B. Bertrand, B. Fabre, J. Higuet, H. Ruf, A. Dubrouil, S. Patchkovskii, M. Spanner, Y. Mairesse, V. Blanchet, E. Mevel, E. Constant, P. B. Corkum, and D. M. Villeneuve, Science **334**, 208 (2011).
[13] B. Wolter, M. G. Pullen, A.-T. Le, M. Baudisch, K. Doblhoff-Dier, A. Senftleben, M. Hemmer, C. D. Schröter, J. Ullrich, T. Pfeifer, R. Moshammer, S. Gräfe, O. Vendrell, C. D. Lin, and J. Biegert, Science **354**, 308 (2016).
[14] P. Cörlin, A. Fischer, M. Schönwald, A. Sperl, T. Mizuno, U. Thumm, T. Pfeifer, and R. Moshammer, Phys. Rev. A **91**, 043415 (2015).
[15] S. De, I. A. Bocharova, M. Magrakvelidze, D. Ray, W. Cao, B. Bergues, U. Thumm, M. F. Kling, I. V. Litvinyuk, and C. L. Cocke, Phys. Rev. A **82**, 013408 (2010).

[16] S. De, M. Magrakvelidze, I. A. Bocharova, D. Ray, W. Cao, I. Znakovskaya, H. Li, Z. Wang, G. Laurent, U. Thumm, M. F. Kling, I. V. Litvinyuk, I. Ben-Itzhak, and C. L. Cocke, Phys. Rev. A **84**, 043410 (2011).

[17] M. Magrakvelidze, C. M. Aikens, and U. Thumm, Phys. Rev. A **86**, 023402 (2012).

[18] X. M. Tong, Z. X. Zhao, and C. D. Lin, Phys. Rev. A **66**, 033402 (2002).

[19] B. Feuerstein and U. Thumm, J. Phys. B **36**, 707 (2003).

[20] C. M. Marian, R. Marian, S. D. Peyerimhoff, B. A. Hess, R. J. Buenker, and G. Seger, Mol. Phys. **46**, 779 (1982).

[21] F. Aquilante, J. Autschbach, R. K. Carlson, L. F. Chibotaru, M. G. Delcey, L. De Vico, I. Fdez. Galvan, N. Ferre, L. M. Frutos, L. Gagliardi, M. Garavelli, A. Giussani, C. E. Hoyer, G. Li Manni, H. Lischka, D. Ma, P. A. Malmqvist, T. Muller, A. Nenov, M. Olivucci, T. B. Pedersen, D. Peng, F. Plasser, B. Pritchard, M. Reiher, I. Rivalta, I. Schapiro, J. Segarra-Marti, M. Stenrup, D. G. Truhlar, L. Ungur, A. Valentini, S. Vancoillie, V. Veryazov, V. P. Vysotskiy, O. Weingart, F. Zapata, and R. Lindh, J. Comput. Chem. **37**, 506 (2016).

[22] X. Zhang, D. Shi, J. Sun, and Z. Zhu, Mol. Phys. **109**, 1627 (2011).

[23] P. Baltzer, B. Wannberg, L. Karlsson, M. Carlsson Göthe, and M. Larsson, Phys. Rev. A **45**, 4374 (1992).

[24] F. R. Gilmore, R. R. Laher, and P. J. Espy, J. Phys. Chem. Ref. Data **21**, 1005 (1992).

[25] J. Yao, S. Jiang, W. Chu, B. Zeng, C. Wu, R. Lu, Z. Li, H. Xie, G. Li, C. Yu, Z. Wang, H. Jiang, Q. Gong, and Y. Cheng, Phys. Rev. Lett. **116**, 143007 (2016).

[26] Y. Liu, Y. Brelet, G. Point, A. Houard, and A. Mysyrowicz, Opt. Express **21**, 22791 (2013).

[27] H. Xu, E. Lötstedt, A. Iwasaki, and K. Yamanouchi, Nat. Commun. **6**, 8347 (2015).

[28] Y. Song, M. Evans, C. Y. Ng, C.-W. Hsu, and G. K. Jarvis, J. Chem. Phys. **112**, 1306 (2000).

[29] K. Sändig, H. Figger, and T. W. Hänsch, Phys. Rev. Lett. **85**, 4876 (2000).

[30] K. P. Huber and G. Herzberg, *Molecular Spectra and Molecular Structure — IV. Constants of Diatomic Molecules* (Van Nostrand Reinhold, New York, 1979).

[31] M. Zohrabi, J. McKenna, B. Gaire, N. G. Johnson, K. D. Carnes, S. De, I. A. Bocharova, M. Magrakvelidze, D. Ray, I. V. Litvinyuk, C. L. Cocke, and I. Ben-Itzhak, Phys. Rev. A **83**, 053405 (2011).

[32] Y. Lu, Z. He, J. Cutler, S. Southworth, W. Stolte, and J. Samson, J. Electron Spectrosc. Relat. Phenom. **94**, 135 (1998).

[33] X. Tang, X. Zhou, M. Niu, S. Liu, and L. Sheng, J. Phys. Chem. A **115**, 6339 (2011).

[34] M. Evans, S. Stimson, C. Y. Ng, C.-W. Hsu, and G. K. Jarvis, J. Chem. Phys. **110**, 315 (1999).

[35] M. Richard-Viard, O. Dutuit, M. Lavollee, T. Govers, P. M. Guyon, and J. Durup, J. Chem. Phys. **82**, 4054 (1985).

[36] E. Goll, G. Wunner, and A. Saenz, Phys. Rev. Lett. **97**, 103003 (2006).

[37] T. Ergler, B. Feuerstein, A. Rudenko, K. Zrost, C. D. Schröter, R. Moshammer, and J. Ullrich, Phys. Rev. Lett. **97**, 103004 (2006).